Red blood cell lingering modulates hematocrit distribution in the microcirculation

Yazdan Rashidi,[1,*] Greta Simionato,[1,2] Qi Zhou,[3] Thomas John,[1] Alexander Kihm,[1] Mohammed Bendaoud,[1,4,5] Timm Krüger,[3] Miguel O. Bernabeu,[6,7] Lars Kaestner,[1,8] Matthias W. Laschke,[2] Michael D. Menger,[2] Christian Wagner,[1,9] and Alexis Darras[1,*]

[1]Experimental Physics, Saarland University, Saarbruecken, Germany; [2]Institute for Clinical and Experimental Surgery, Saarland University, Homburg, Germany; [3]School of Engineering, Institute for Multiscale Thermofluids, University of Edinburgh, Edinburgh, United Kingdom; [4]Université Grenoble Alpes, CNRS, LIPhy, Grenoble, France; [5]LaMCScI, Faculty of Sciences, Mohammed V University of Rabat, Rabat, Morocco; [6]Centre for Medical Informatics, Usher Institute, University of Edinburgh, Edinburgh, United Kingdom; [7]The Bayes Centre, University of Edinburgh, Edinburgh, United Kingdom; [8]Theoretical Medicine and Biosciences, Saarland University, Homburg, Germany; and [9]Physics and Materials Science Research Unit, University of Luxembourg, Luxembourg, Luxembourg

ABSTRACT   The distribution of red blood cells (RBCs) in the microcirculation determines the oxygen delivery and solute transport to tissues. This process relies on the partitioning of RBCs at successive bifurcations throughout the microvascular network, and it has been known since the last century that RBCs partition disproportionately to the fractional blood flow rate, therefore leading to heterogeneity of the hematocrit (i.e., volume fraction of RBCs in blood) in microvessels. Usually, downstream of a microvascular bifurcation, the vessel branch with a higher fraction of blood flow receives an even higher fraction of RBC flux. However, both temporal and time-average deviations from this phase-separation law have been observed in recent studies. Here, we quantify how the microscopic behavior of RBC lingering (i.e., RBCs temporarily residing near the bifurcation apex with diminished velocity) influences their partitioning, through combined in vivo experiments and in silico simulations. We developed an approach to quantify the cell lingering at highly confined capillary-level bifurcations and demonstrate that it correlates with deviations of the phase-separation process from established empirical predictions by Pries et al. Furthermore, we shed light on how the bifurcation geometry and cell membrane rigidity can affect the lingering behavior of RBCs; e.g., rigid cells tend to linger less than softer ones. Taken together, RBC lingering is an important mechanism that should be considered when studying how abnormal RBC rigidity in diseases such as malaria and sickle-cell disease could hinder the microcirculatory blood flow or how the vascular networks are altered under pathological conditions (e.g., thrombosis, tumors, aneurysm).

SIGNIFICANCE   We demonstrate in vivo that the lingering behavior of red blood cells (RBCs) at the apex of bifurcations modulates their partitioning in the microcirculation. The influence of this mechanism opens new ways of understanding how altered RBC properties in pathologies can hinder the microvascular blood flow, or influence the development or remodeling of the vascular networks. For instance, we show that rigid RBCs linger less at typical Y-shaped bifurcations and manifest a distribution pattern closer to the well-known Zweifach-Fung effect. We also highlight certain properties of the bifurcation geometry that contribute to the lingering intensity of RBCs.

INTRODUCTION

Partitioning of red blood cells (RBCs) through bifurcations of blood vessels determines how the oxygen is delivered to tissues and organs. Early studies have shown that this partitioning is a complex phenomenon (1–4) and, since then, it has been an area of intensive research, attracting a wide range of experimental (5–13) and numerical (14–20) studies. More accurately, vessels with a higher flow rate tend to collect an even higher proportion of RBCs. This fact is known as the Zweifach-Fung effect and leads to heterogeneity in the hematocrit between various vessels (2). Uncovering the mechanisms for such a partitioning behavior is crucial to understand not only the transport of oxygen and solutes across vascular networks but also the development or remodeling of the networks themselves, as RBC dynamics were recently discovered to

underpin vessel remodeling, presumably by mediating the wall shear stress difference between neighboring branches via the route of effective blood viscosity (21).

An empirical model that effectively recapitulates the time-average behavior of the Zweifach-Fung effect was developed by Pries et al. in the 1990s (22–24) and has been widely employed by the research community for studying microvascular blood flow. However, recent in vitro and in silico studies demonstrated that notable deviations from this empirical model can arise for various reasons (5,7,8,10,25,26). In particular, it has been shown that RBC partitioning at bifurcations in the smallest vessels of the microvascular network tend to deviate from the empirical predictions more severely (11,12,21,27,28). On the other hand, first established through numerical simulations (25) and subsequently validated by in vivo experiments (29), an intriguing behavior of RBCs in the microvasculature was highlighted: they linger at the apex of bifurcations (i.e., the cells temporarily residing near the branching point of vessels with diminished velocity) for certain periods of time, consequently modifying the dynamics of cells entering downstream vessels and the characteristic inter-cell distances featuring intermittent voids.

Previously, Bagchi et al. (25) extensively characterized the time-dependent correlation between single-cell lingering times and geometry of the network, but the causal relationship between the lingering pattern and the average behavior of RBC distribution through the bifurcation was not explicitly investigated. Their following work (28) further combined a continuum model with the cellular simulation to distinguish the effects of plasma skimming and cell screening. More recently, Bagchi et al. reported how changes in the fraction of lingering population between rigidified and healthy cells are related to deviations from identity of the RBC flow rate and overall blood flow rate (30). Notwithstanding the progress above, a mechanistic understanding of the deviation from identity due to the Zweifach-Fung effect as well as the baseline behavior of how such deviations are associated with the proportion or absolute residence time of lingering cells is yet to be obtained.

In the present study, we systematically analyze how the lingering of RBCs influences their partitioning at highly confined capillary-level bifurcations in the microcirculation (where the cells literally squeeze themselves through and negligible cell-free layer exists contrary to prior studies; cf. (22–24)). Through carefully designed in vivo experiments corroborated by complementary in silico simulations on timescales longer than the lingering time and relevant for physiological conditions, we show that global deviations from the empirical model by Pries et al. (24) are strongly correlated with normalized average duration of cell lingering events. We further reveal how lingering modulates RBCs partitioning, with a primary focus on mechanistic understanding of the deviation from the baseline behavior of Zweifach-Fung effect as postulated by the empirical model (24). The asymmetric drive

from RBC lingering is found to either reinforce or revert the Zweifach-Fung effect. In addition, given that RBCs usually exhibit large deformations when lingering, we also investigate numerically how cells with increased stiffness differ from healthy ones in their lingering and partitioning behavior. Our results demonstrate that RBC lingering is a cause of statistical deviation from the Zweifach-Fung partitioning and provide further evidence that pathologically rigidified cells can impair the distribution of RBCs across the microcirculation (31–38) due to altered lingering properties.

MATERIALS AND METHODS

In vivo experiments

Permissions

Experiments were performed in Syrian golden hamsters according to the German legislation on protection of animals and were approved by the local governmental animal protection committee (permission number 25/2018). Hamsters were maintained on a standard 12/12 h day/night cycle and water and food were provided ad libitum. Detailed methods are described below for each type of investigation.

Animal preparation and microscopy

Hamsters with an age of 5–7 weeks, weighing 55–70 g, were used for the implantation of a dorsal skinfold chamber (39). The surgery was performed under deep anesthesia (150 mg/kg ketamin (Serumwerke Bernburg AG)/ 0.25 mg/kg domitor (Orion Pharma) intraperitoneal), with intraoperative pain medication by carprofen (10 mg/kg, Zoetis, subcutaneous). A previously described protocol (39) was followed. Briefly, the back of the hamsters was shaved and a titanium chamber consisting of two frames was implanted on the lifted dorsal skinfold. On the frame with a circular observation window (diameter of 10 mm) the cutis, subcutis, and retractor muscle were removed to expose the striated skin muscle for later observation of the microcirculation. The window was closed with a cover glass that was fixed with a snap ring. An implanted dorsal skinfold chamber is depicted in Fig. 1 a. Animals were allowed to recover for 72 h after the procedure.

Hamsters were anesthetized as described above before intravital microscopy. A volume of 100 μL of the fluorescent plasma marker fluorescein isothiocyanate (FITC)-labeled (5%, 150 kDa, Sigma-Aldrich) was injected retro-orbitally and the animals were fixed on a Plexiglas stage, as illustrated in Fig. 1 b. Several capillary bifurcations in different areas of the chamber window were chosen for epifluorescence microscopy (Axio Examiner A1, Zeiss). FITC-labeled dextran was excited with a 480-nm light-emitting diode (LED) (Colibri 7, Zeiss), and image contrast was additionally enhanced by simultaneously using transmitted blue light, which is absorbed by hemoglobin, making RBCs appear darker. Imaging was performed with 20× (LD A-Plan, NA = 0.35, Zeiss), 50× (LD EC Epiplan-Neofluar, NA = 0.55, Zeiss), or 100× (LD C Epiplan-Neofluar 100×, NA = 0.75, Zeiss) long-distance objectives. Video acquisition was carried out with a digital camera (Hamamatsu Orca Flash 4.0, C13440) using the software ZEN 3.1 Blue (Zeiss). For each video, 2000 frames were recorded at different rates according to flow velocity (100–170 Hz). A 2 × 2 binning was applied during acquisition. An example of an obtained image is given in Fig. 1 c.

Image analysis and lingering quantification

Despite the animal being fixed on the Plexiglas stage, its breathing and/or muscles movement caused slight translations of the microscopic field of view in the image sequence (Fig. S1 a). To determine the motion of the RBCs in the vessels, we first correct those translations by translating each image by the maximum of its 2D correlation with the first image in
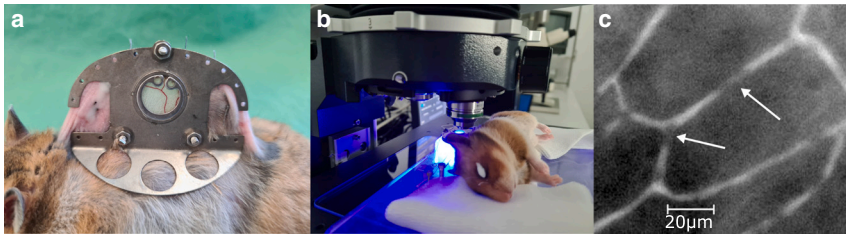
FIGURE 1 Experimental methods. (*a*) Dorsal skinfold chamber implanted on the back of a hamster. (*b*) Anesthetized hamster placed underneath the objective of an epifluorescence microscope. (*c*) An exemplar microvascular network imaged by fluorescence microscopy. The dyed plasma appears bright; RBCs in capillaries (see arrows) and the surrounding tissues are dark. To see this figure in color, go online.

the sequence. This process creates a movie where the vessels and surrounding tissues are still fixed (see Fig. S1 *b*). A Gaussian filter (with standard deviation of two pixels) is then applied to despeckle the images, and a mask is drawn around the vessels. The creation of this mask is facilitated by also considering the image showing the standard deviation of each pixel intensity along time, which is higher in the vessels with transient (dark) RBCs and offers a guide to the eye for the mask drawing (see Fig. S1 *c*). The diameters D of the various vessels are computed as twice the average distance from the skeleton pixels of the masks to the border of the vessels, using standard Matlab functions bwmorph and bwdist (see Fig. S1 *c*). The image series is then inverted and binarized inside the mask area with a threshold based on a user-defined fraction of the Otsu threshold (40). The Otsu thresholding method was used because the average intensity of images is usually slightly flickering. However, the automated threshold algorithm overestimated the threshold required to detect the whole RBCs; hence, we implemented a user-defined ratio to adjust it (see Fig. S1 *d*).

The hematocrit H was calculated based on the binarized image: $H = \varphi_s \frac{V_{RBC}}{A_{RBC}\pi R_v}$, where φ_s is the measured average area fraction of RBCs in the vessel, $V_{RBC} = 56.5\mu m^3$ and A_{RBC} are the cell volume and the surface area (measured empirically in each vessel for a selection of single cells) of the RBCs respectively, and R_v is the vessel radius. This correction, similar to the approach in previous work (7), takes into account the deformation of the cells in the plane while avoiding any counting mistake that close RBCs (or the segmentation algorithm) could induce (see Supporting material for more details). This correction is validated using 2D projection slices of the numerical simulation, where the hematocrit value is known as simulation input; the error for the validation is below 1%. For detected RBCs, the standard Matlab function WeightedCentroid was used to calculate their center of mass. In this function, the center of mass is calculated based on the location and intensity $\vec{R} = \sum_{i=1}^{N}\sum_{j=1}^{N}[x_i,y_j]I(x_i,y_j)/\sum_{i=1}^{N}\sum_{j=1}^{N}I(x_i,y_j)$, where x and y are the coordinates of each pixel and $I(x,y)$ refers to the intensity of the pixel at position $[x,y]$.

A tracking algorithm was then used to determine the velocity of the detected RBCs (41). The variations of light intensity along the vessels, in conjunction with the collisions and transient aggregations of RBCs, did not allow us to reliably follow all RBCs along their entire trajectories. However, as we focused on bifurcations where the mother vessel (M) and the two daughter vessels have a hematocrit low enough to distinct single RBCs, this tracking allowed us to extract the spatial distribution of the RBC velocity (i.e., we performed particle tracking velocimetry (PTV)), on which we performed our further analyses. In this article, we will refer to the two daughter vessels as main daughter (MD) and secondary daughter (SD). By definition, MD is the daughter vessel with higher fractional blood flow rate and SD is the one with lower value.

To detect the lingering of RBCs, we applied a method as in our prior work (29) by defining a circle with a diameter of 6 μm (i.e., the main diameter of a hamster RBC) surrounding the bifurcation apex (Fig. 3 *a*). The cells were considered to linger if their center of mass was located in this circle and at the same time had a velocity lower than the local minimum detected in the probability density function (PDF) of a collective dataset of RBC velocities (Fig. 3 *b*). The velocity PDF displayed in Fig. 3 *b* was obtained by considering the M vessel and the bifurcation area. In this study, flow and cell statistics were characterized within specific time intervals

(10–20 s), longer than the transit time of individual RBCs but still short enough so that the flow is quasi-steady (i.e., no systematic trend and/or significant change in the volume flow rates can be identified). Within such intervals, self-consistent observables could be well defined.

Numerical simulations

Complementary simulations for time-dependent RBC flow in the representative capillary bifurcations were run with *HemeLB* (https://github.com/hemelb-codes/hemelb) using the immersed-boundary-lattice-Boltzmann method following our previous approach (21). First, three-dimensional (3D) luminal surface models were reconstructed from binary masks of the capillary bifurcations using open-source software *PolNet* (42), assuming circular cross sections of varying diameter along each vessel. Then the flow domain enclosed by the luminal surface was uniformly discretized into cubic lattices of fine voxel size $\Delta x = 0.25\ \mu m$, aimed at resolving cell dynamics with high resolution at the bifurcation apex. To initialize the simulation, inflow/outflow boundary conditions based on experimental time-average volume flow rates were imposed at the end of the M vessel and the MD branch (similarly defined as above for the experiments) of each bifurcation, and a reference pressure for the SD branch. No-slip boundary conditions were imposed at the vessel wall. The physical length corresponding to each simulation time step was $\Delta t = 1.04 \times 10^{-6}s$.

The simulation for each bifurcation was initialized with (RBC-free) plasma flow. Once the plasma flow became converged, RBCs were randomly inserted from the M vessel through a cylindrical flow inlet with constant feeding hematocrit (H_F) as measured from experiments (see Supporting material section "simulation hematocrit and RBC initialization"). When RBCs reached the end of MD or SD, they were removed from the simulation domain. Each RBC was modeled as a cytosol-filled capsule with an isotropic and hyperelastic membrane consisting of 5120 triangular facets. The mechanical properties of the RBCs were governed by elastic moduli governing different energy contributions, such as shearing and bending of the membrane. The cytosol was treated as a Newtonian fluid with the same viscosity as the suspending medium (i.e., blood plasma). The viscosity of the RBC membrane itself was not considered. To probe the effect of confinement, two different RBC diameters were considered ($D_{rbc} = 6\ \mu m$ corresponding to normal hamster RBC size and $D_{rbc} = 8\ \mu m$ corresponding to larger cells of similar size to a human RBC). Two different membrane stiffness levels (stain modulus $\kappa_s = 5 \times 10^{-6}, 5 \times 10^{-5}N/m$) were considered for representing a normal and a hardened cell, respectively. For cell-cell and cell-wall interactions, repulsive potentials inversely decaying with the distance were implemented. High-enough resolution was used to ensure the cell-cell/cell-wall distance did not fall below one grid point.

RESULTS AND DISCUSSION

Determination of flow rates and baseline Zweifach-Fung partitioning

To determine how the lingering of RBCs influences their partitioning, we used the empirical model of Pries et al.

for the Zweifach-Fung effect (24) as a baseline. For this purpose, we first determined the blood flow rate Q in each vessel. Since the vessels were smaller than the main radius of the RBCs, we assumed a plug flow. We also assumed that the difference between the tube and discharge hematocrits was negligible in our observations. The flow rates within all bifurcation segments were therefore initially assessed from the velocities (V) and diameter (D) measurements of the individual segments

$$\langle Q \rangle = \langle V \rangle \pi \left(\frac{D}{2}\right)^2, \tag{1}$$

similarly to previous studies (22,29,43). Mass conservation stipulates that the total volume flow rate from the M vessel Q_M is divided into the daughter branches and satisfy $Q_M = Q_{MD} + Q_{SD}$. The subscripts MD and SD refer to the main daughter and secondary daughter, respectively. To obey this conservation law and minimize experimental errors, values obtained from Eq. 1 were corrected following the normalization process described by Pries et al. in previous similar measurements (22). Similarly, the measured erythrocyte flow rates $E_i = H_i Q_i$, H_i being the local hematocrit, were also corrected to obey $E_M = E_{MD} + E_{SD}$. The empirical law for the Zweifach-Fung effect developed by Pries et al. (22–24) describes the relation between fractional blood flow, FQ_b, and the fractional erythrocyte flux, FQ_e, in the microvascular bifurcation. The fractional blood flows FQ_b for both daughter vessels were calculated by dividing the flow rate Q in the respective daughter by the flow rate in the M vessel. The fractional erythrocyte flow rates FQ_e were computed as the ratio of the corrected erythrocytes flow rates (e.g., E_{MD}/E_M for the MD). With these definitions, the model from Pries et al. (22–24) states

where H refers to the measured hematocrit, calculated from the average area fraction of RBCs in the mask during the experiment (23,24). The subscripts indicate the vessel for which the quantity is considered.

Due to the heterogeneous blood flow and diverse geometries in the microvasculature, the FQ_e and FQ_b data extracted in vivo are naturally scattered (22,23), which may also apply for regular in vitro vascular networks (10,11). However, Pries et al. derived their empirical model for robust single-bifurcation predictability (see Fig. 4 in Ref. (22) and Fig. 2 in Ref. (23)) with in vivo data obtained through a classic protocol that enabled continual variation of the hematocrits in individual bifurcations.

In the present study, we set out to investigate why individual bifurcation cases (a widely adopted approach (5–8, 16–18) to study the RBC partitioning behavior) would nicely scatter around this empirical limit as defined by Eq. 2, bearing in mind that the effects of flow ratio, vessel geometry, and feeding hematocrit were already accounted for in the original model. To do this experimentally, we consider a set of bifurcations selected in vivo to examine how the RBC partitioning in them deviates from the baseline split (as postulated by Eq. 2) and further correlate the deviation with experimental factors not considered by the empirical model. In particular, we focus on the lingering behavior, which appears a potential mechanism for such deviations in highly confined capillaries. Indeed, the initial study of Pries et al. analyzed arteriolar bifurcations with characteristic diameters about 8 μm or larger (22); i.e., larger than the main diameter of hamster RBCs. In their studies of bifurcations with lower confinement level, the lingering behavior (if any) was probably not playing a significant role in the partitioning of cells. In the case presented here, studied vessel diameters range between 3.5

$$FQ_e = \begin{cases} 0, & \text{if } FQ_b < X_0 \\ 1, & \text{if } FQ_b > 1 - X_0 \\ \text{logit}^{-1}\left(A + B \, \text{logit}\left(\frac{FQ_b - X_0}{1 - 2X_0}\right)\right), & \text{otherwise} \end{cases} \tag{2}$$

where $\text{logit}(x) = \ln(x/(1-x))$ and A, B, X_0 are related to the bifurcation geometry and feeding hematocrit in the M:

and 5.6 μm; i.e., considerably smaller than the diameter of the hamster RBCs. Such high confinement would favor

$$A_{MD} = -13.29 \frac{D_{MD}^2/D_{SD}^2 - 1}{D_{MD}^2/D_{SD}^2 + 1}(1 - H_M)\bigg/ D_M, A_{SD} = -A_{MD}, B = 1 + 6.98\left(\frac{1 - H_M}{D_M}\right), X_0 = 0.964\left(\frac{1 - H_M}{D_M}\right), \tag{3}$$
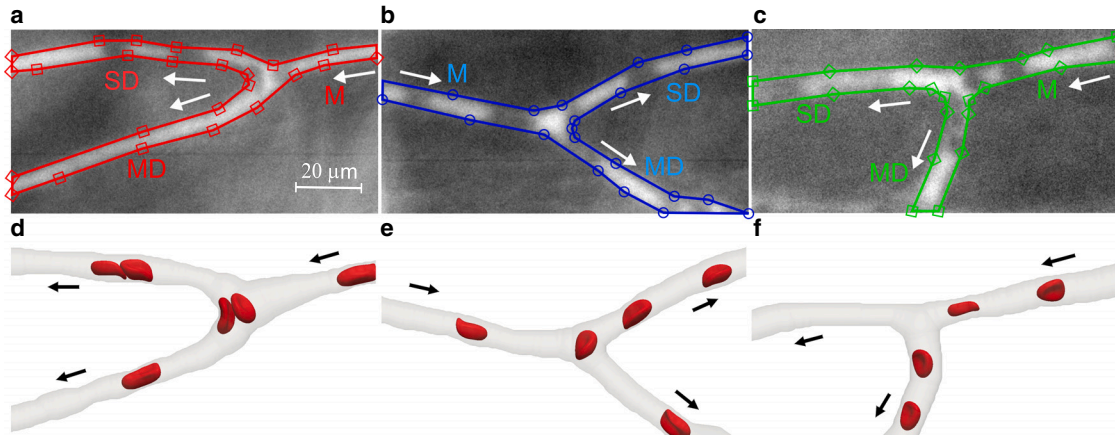
FIGURE 2 Representative bifurcations from experiments that are simulated. (*a–c*) Three bifurcations selected from the experiments hereafter referred to as BIF-a, BIF-b, and BIF-c, respectively. The M vessel, the MD, and SD are annotated with arrows indicating the flow direction. The plasma was stained with fluorescent dye (bright in the images). Dark areas in the vessels indicate the RBCs. The border of the masks used to analyze the bifurcations are depicted in colored symbols. Consistent colors and symbols are used for these bifurcations throughout the article. (*d–f*) Simulated RBC flow in the reconstructed domain of cropped bifurcations, respectively (*a–c*) as characterized experimentally. To see this figure in color, go online.

the lingering of RBCs as the cells cannot easily avoid interacting with the vessel wall at the bifurcation.

Lingering and partitioning

Global description

Experiments. Fig. 2 *a–c* shows three representative bifurcations (two Y shaped and one T shaped) where all required parameters could be extracted from the image sequences. A characteristic movie is provided as Video S1. We calculated the empirical predictions by Eq. 2 for each bifurcation (nine in total) and defined the deviations from the model as $\delta ZF = \left| \Delta FQ_e^{EX} - \Delta FQ_e^{ZF} \right|$. Alternative definitions of the deviation (e.g., in signed form ΔZF) are discussed in the Supporting material (Fig. S7). We noted $\Delta FQ_e = FQ_{e(MD)} - FQ_{e(SD)}$, the difference of fractional erythrocyte

flow rate, and the expressions *EX* and *ZF* refer to the experimental data and the empirical prediction, respectively. The fractional blood flow rate FQ_b is given by the experimental measurements, and the predicted fractional erythrocyte flow rate FQ_e^{ZF} is computed through Eq. 2 (see Fig. 4 *a* for a schematic).

To quantify the lingering of RBCs at each bifurcation, we first determined the average duration of the lingering events $\langle \tau \rangle$. The total lingering time was considered as the sum of the duration of all detected lingering events. We then determined the ratio of this total lingering time to the number of the RBCs as the characteristic average lingering time $\langle \tau \rangle$. Since this time is highly correlated with the flow rate and the transit time of an RBC through the bifurcation (i.e., the red circle defined in Fig. 3 *a*), we normalized it by $t_s = R/\langle V_M \rangle$. The radius $R = 3$ μm is the radius of the red circle defined in Fig. 3 *a* and V_M the average velocity in the M vessel.
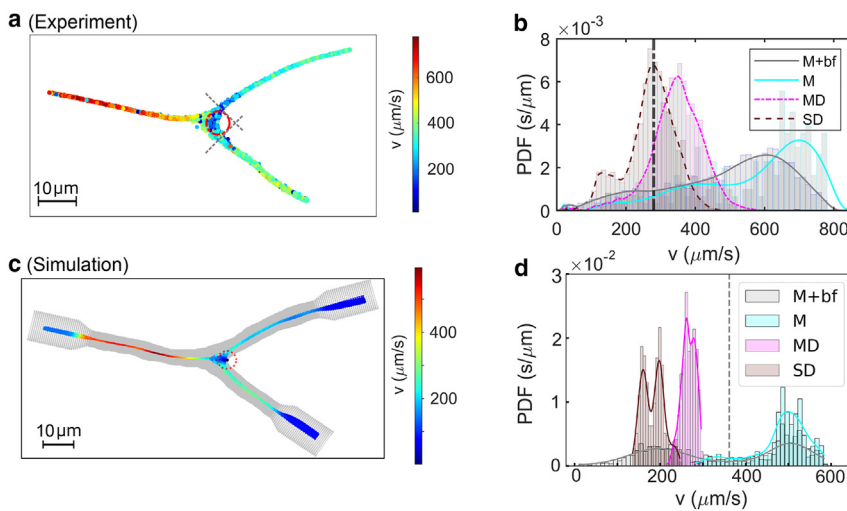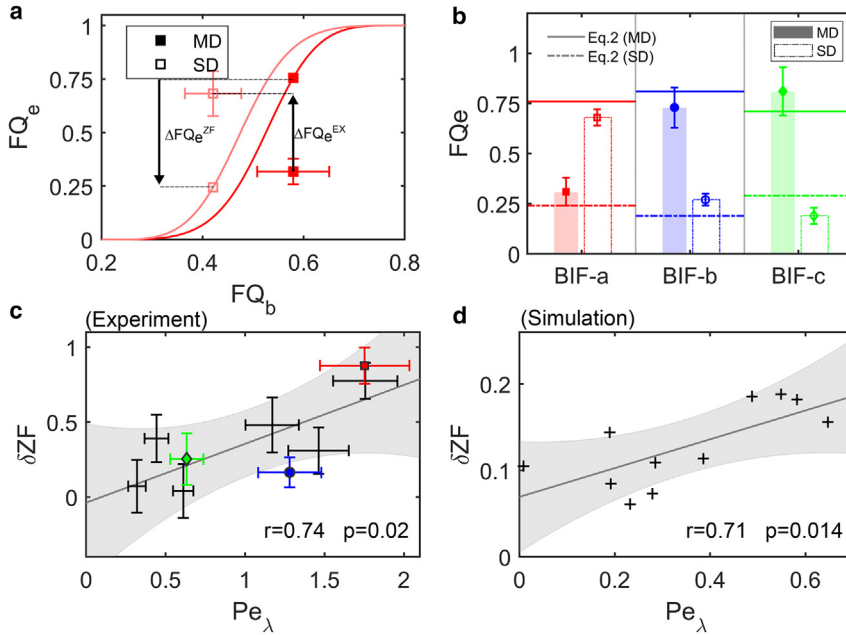

FIGURE 3 RBC velocity distributions in the experiment and simulation. (*a*) Spatial distribution of RBC velocities obtained through particle tracking in experiment for BIF-b. Lingering is considered to occur if a cell is inside the red circle (6 μm, size of a typical hamster RBC) with a velocity lower than the threshold velocity, which is determined as a local minimum in the PDF of velocities obtained from the M vessel and the bifurcation area (M + bf), as shown in (*b*). For comparison, the velocity PDFs for the MD and SD branches and the M vessel are also shown. (*c*) Corresponding color map of RBC velocities measured along simulated cell trajectories in BIF-b. (*d*) Velocity PDFs measured in different vessel branches of the simulated BIF-b as for the experimental data in (*b*). To see this figure in color, go online.

FIGURE 4 Experimental and simulation results of RBC partitioning versus lingering. (*a*) Comparison of experimental RBC partitioning against the empirical predictions of the Zweifach-Fung effect (for BIF-a as in Fig. 2 *a*). The axes FQ_e and FQ_b are for the fractional RBC flux and fractional blood flow, respectively. The deviation from the empirical prediction was calculated as $\delta ZF = \left| \Delta FQ_e^{EX} - \Delta FQ_e^{ZF} \right|$. (*b*) The bars show experimental results against the lines, representing empirical predictions by Eq. 2. The data here are for the three characteristic bifurcations in Fig. 2 *a–c*, with consistent colors and symbols. Dashed lines and hollow symbols here refer to the SD vessel with lower fractional flow rate FQ_b. Note the inversion of the Zweifach-Fung effect in BIF-a. (*c*) Experimental deviation δZF from Eq. 2 as a function of the lingering Péclet number Pe_λ. The points with error bars are experimental data, and the solid line shows linear regression fitting of the data points, with the shaded area indicating 95% confidence interval prediction from the fit. All data gathered from nine bifurcations (including the three bifurcations BIF-a, BIF-b, and BIF-c in Fig. 2 *a–c*) are included in this graph. The Pearson-*r* correlation coefficient (n = 9) is $r = 0.74$ ($p = 0.02$). Error bars in (*a–c*) are computed by error propagation from the underlying experimental measurements. (*d*) Correlation between δZF and Pe_λ in simulations (n = 12). The crosses are simulation data and the solid line shows linear regression fitting of the data points. The Pearson-*r* correlation coefficient is $r = 0.71$ ($p = 0.014$). To see this figure in color, go online.

The time t_s is then a characteristic advection time that a cell would need to go through the lingering detection area (where the cell velocities diminish; Fig. 3 *b*). We defined the ratio of these two characteristic times as $Pe_\lambda = \langle \tau \rangle / t_s$. The ratio Pe_λ defines the equivalent of a Péclet number, since it compares two characteristic times of different transport modes at the bifurcation (lingering and advection). As shown in Fig. 4 *c* for nine different bifurcations (see experimental details in Table S1), the deviation δZF from the Zweifach-Fung prediction Eq. 2 strongly correlates with Pe_λ (Pearson correlation coefficient $r = 0.74$, $p < 0.05$).

Interestingly, we observed in some case that the deviation from the Zweifach-Fung effect caused by the lingering can revert the partitioning. Indeed, in the case of the (red) characteristic bifurcation highlighted in Fig. 2 *a*, the MD (with higher FQ_b) is the branch with lower FQ_e. This is often referred to in the literature as reverse partitioning (7,10,11,26). In our data, we only observed such reverse partitioning for the highest $Pe_\lambda \approx 1.75$.

Simulations. The three representative bifurcations from experiments in Fig. 2 *a–c* were also simulated under equivalent flow conditions and RBC volume fractions (see details in Table S1), with the lingering phenomenon of RBCs successfully reproduced (Fig. 2 *d–f*). These bifurcations were selected for numerical scrutiny because their experimental counterparts roughly cover the entire range of primary observables (e.g., Pe_λ, δ_{ZF}, dp_τ). A compilation of animation videos generated from numerical simulations are provided as Video S2. To quantify the lingering behavior, an equivalent procedure to the experimental data analysis was applied to analyze the simulation data too. Exemplar trajectories of RBCs near the bifurca-

tion apex from simulations of varying feeding hematocrits are shown in Fig. S3.

In line with the experimental PTV measurements, the cell velocities diminished as the RBCs approached the bifurcation apex (Fig. 3 *c*). After entering one of the daughter branches (*MD* or *SD*), the instantaneous velocity of RBCs would increase again. These patterns were well captured by the velocity PDFs compiled for individual vessel branches in each bifurcation (Fig. 3 *d*). Quantification of lingering events based on the simulated RBC velocities revealed that the percentages of lingering cells for the three bifurcations were 63%, 85%, and 4%, respectively. For hardened RBCs with a membrane strain modulus 10 times as large, the ratios became 23%, 77%, and 42%. Note that the proportion of lingering cells does not unequivocally determine Pe_λ; rather, the average lingering time dominates, considered as the sum of time duration (monitored from all detected lingering events) divided by the total number of cell transits. In other words, a higher proportion of lingering cells does not necessarily lead to a higher Péclet number. For instance, a lower portion of cells lingers in BIF-a than in BIF-b, but they linger for longer time compared with their advection time, therefore causing a larger Pe_λ.

The correlation between the lingering intensity of RBCs and their partitioning at the bifurcations, namely Pe_λ and δZF, was evaluated similarly to the experimental data (Fig. 4 *d*). A strong association was found, indicating a linear increase of δZF against Pe_λ (Pearson-*r* correlation coefficient 0.71, $p < 0.05$). Nevertheless, the absolute magnitude of δZF and Pe_λ were substantially smaller (although in a proportional manner) than their experimental counterpart in Fig. 4 *c*. The
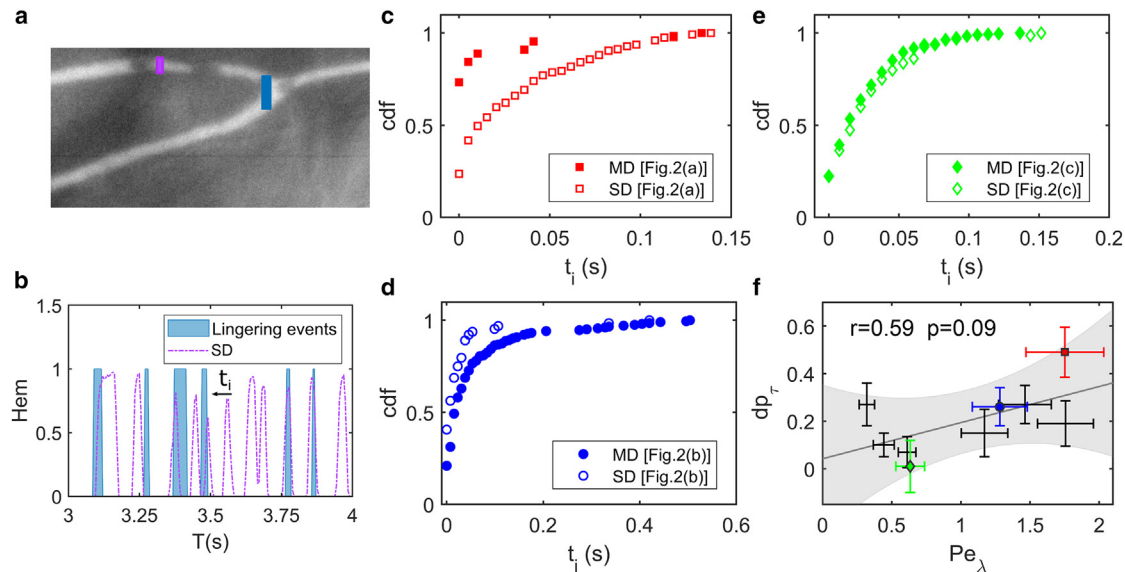
FIGURE 5 Asymmetry in RBC lingering at the bifurcation. (a) Example of mask set used to determine the advection time t_a of RBCs from the bifurcation (blue mask) to the SD branch (magenta mask) via convolution of the hematocrit in both masks (see main text and Fig. S2). Equivalent analysis is performed independently for the MD branch. (b) Extraction of the proximity time t_i of each cell. The hematocrit variation over time, extracted from the daughter's mask, is first translated by the average advection time t_a (see Fig. S2). Then, for each peak of this hematocrit along time, a proximity time t_i is obtained as the temporal distance from the closest lingering event. This process is performed independently for the two daughters. (c–e) CDF of the proximity time to lingering events for both daughters of the three characteristic bifurcations. When a significant difference (considerable dp_τ) is observed in the experiments, higher proportion of lingering cells (and a closer proximity with lingering events) is usually obtained in the daughter branch with the lower fractional RBC flux FQ_e. (f) The correlation between experimental dp_τ (difference in the proportion of lingering cells in SD and MD calculated from CDFs at $t_i = 0$) and Pe_λ. The Pearson-r correlation coefficient is 0.59 ($p = 0.09$). To see this figure in color, go online. Error bars are computed by error propagation from the experimental uncertainties of p_{SD} and p_{MD}.

highest Péclet number was only $Pe_\lambda = 0.65$ in the simulations compared with a maximum value of $Pe_\lambda = 1.75$ in the experiments. This discrepancy may have arisen from simulation configurations that are different from in vivo experiments; e.g., absence of endothelial surface layer (ESL; roughly 0.4–0.5 μm in thickness) and RBC glycocalyx in the numerical model. Indeed, although a repulsive cell-wall potential was implemented, it is possible that the ESL coated by ciliated structures interacts with the RBCs in more complex ways (20,44,45). For instance, it may contribute to enhanced confinement or give rise to an attraction force. Because these advanced cell-wall interactions have not been definitively characterized in the literature, without a tangible physical model, we could not capture such effects in our simulations. In any case, the correlation between the lingering Péclet number Pe_λ and the deviation from the Pries model was qualitatively similar between the experiment and the simulation. We note that no reverse partitioning (or inversion of the Zweifach-Fung effect) was observed in our simulations, which is in agreement with the fact that reverse partitioning in experiments only occurred for bifurcations with $Pe_\lambda > 1.75$.

Lingering asymmetry in experiments

For insights into how the lingering behavior could modify RBC partitioning at the bifurcation, we further examined its symmetry between the two daughter branches. Indeed, as can be seen from Video S1, the RBCs tend to enter the lower daughter branch (MD) almost only if there is another cell already lingering at the bifurcation apex. Due to cell collisions at the apex, it was not possible to precisely determine the proportion of lingering cells entering each daughter merely by analyzing their trajectories. Therefore, we calculated the average advection time t_a of the cells between the (blue) mask in bifurcation and the (magenta) mask in the daughter (Fig. 5 a). This advection time was determined by calculating the convolution of the temporal hematocrit in the daughter mask and that in the bifurcation mask (see Fig. 5 a and Fig. S2 b). We then checked if there was a lingering event at the bifurcation (also monitored in a thin mask) at a time t_a earlier for each cell detection.

We realized that, for such sorting, some lingering events at the bifurcation could not be attributed to any advected cell into the daughters. Indeed, the advection time of each cell can vary slightly, depending on its interactions with other cells near the apex. Therefore, after being temporally translated by t_a, the cell detection can be located close to the lingering event but not exactly within its duration. For more accurate characterization, we therefore measured the proximity time t_i between the closest lingering event and the transit time (detection time in the daughter minus t_a) for each cell (Fig. 5 b). Cells with a proximity time $t_i = 0$ can then be determined as lingering. We further defined $dp_\tau = |p_{SD} - p_{MD}|$ as the difference between the proportion of lingering cells in the two daughter branches (Fig. 5 f).

Because cells with a small proximity time t_i might also have been lingering or might have interacted with another cell lingering at the apex, we used the difference between the first two points of the cumulative density function (CDF) distribution of t_i (Fig. 5 $c-e$) as error bars for p_{SD} and p_{MD}. As can be seen in Fig. 5 $c-e$, the proximity time t_i distribution and the proportion of cells identified as lingering are distinct for the two daughters under large Pe_λ. For the experimentally observed cases as highlighted in Fig. 5 f, the asymmetry in the proportion of lingering cells is weakly correlated with the lingering intensity Pe_λ. In simulation, both dp_τ and Pe_λ for the simulated bifurcations (three in total) are smaller than their experimental counterpart but in a proportional manner with qualitative agreement (see Fig. S2 c).

Origin of lingering in experiments

To understand what causes the cells to linger, we identified geometrical features of the bifurcations correlating with the lingering Péclet number Pe_λ. Due to the definition of the lingering events as a significant reduction of the RBC velocity at the bifurcation, it is likely that cells linger at the stagnation point; i.e., the intersection of the bifurcation's wall and the flow divider plane. Note that a stagnation point is considered because the 3D vessels are projected in the mid-vessel plane. At this position, the cells will also experience the smallest drag force, likely not to push the cell toward any

daughter vessel. The position of the stagnation point depends on the fractional flow rate of the daughter branches (46). The distance of the stagnation point from the center line L_s, which is depicted in the Fig. 6 a, can be approximated through

$$\frac{Q_{MD}}{Q_{SD}} = \frac{1 + \frac{2}{\pi}\arcsin\left(\frac{L_s}{R_M}\right) + \frac{2L_s}{\pi R_M^2}\sqrt{R_M^2 - L_s^2}}{1 - \frac{2}{\pi}\arcsin\left(\frac{L_s}{R_M}\right) - \frac{2L_s}{\pi R_M^2}\sqrt{R_M^2 - L_s^2}}, \quad (4)$$

where R_M is the radius of the M branch (see Supporting material for further justification). For the situations where numerical simulations were compared with the experimental data, positions of the stagnation point determined this way were located within one pixel of distance from the position indicated by the streamlines (see Fig. S4). This approximation can then be considered to be consistent with the available numerical data. Numerical simulations also showed that the shift of the stagnation point due to studied RBC transits were negligible compared with other experimental uncertainties (see Fig. S5).

Since the cells at the stagnation point experience the smallest drag force, one can assume that the dominating forces on the cells arise from their interaction with the endothelial layer. In turn, this interaction probably depends on the geometry of the wall at this location, which can mostly be described through its curvature. To determine the curvature of each bifurcation, a circle was fitted on the neighborhood of the stagnation point
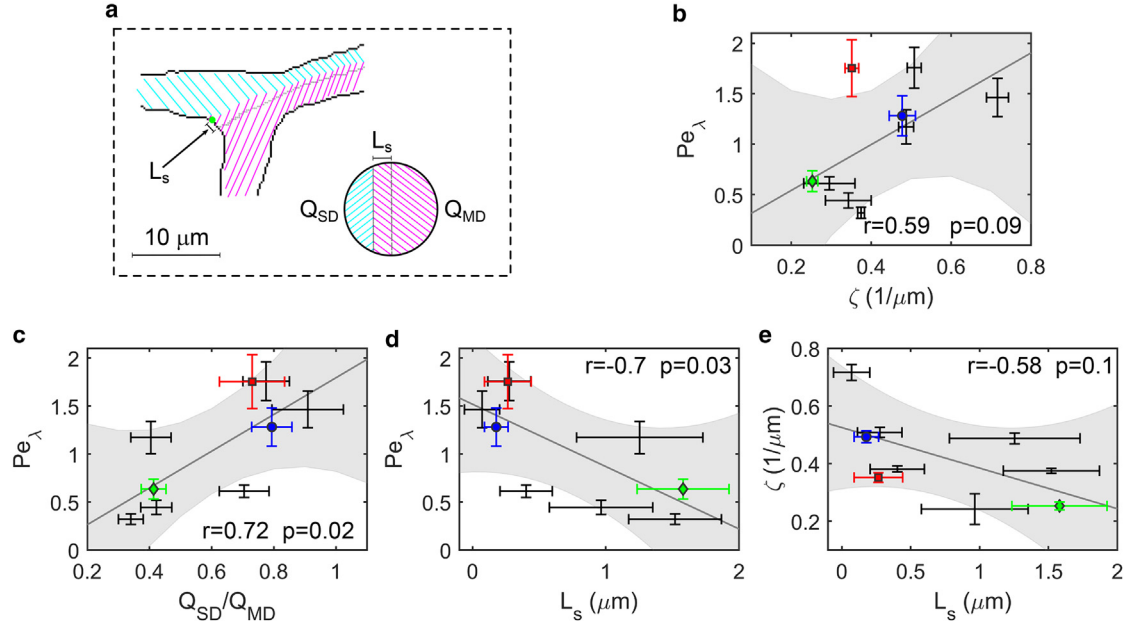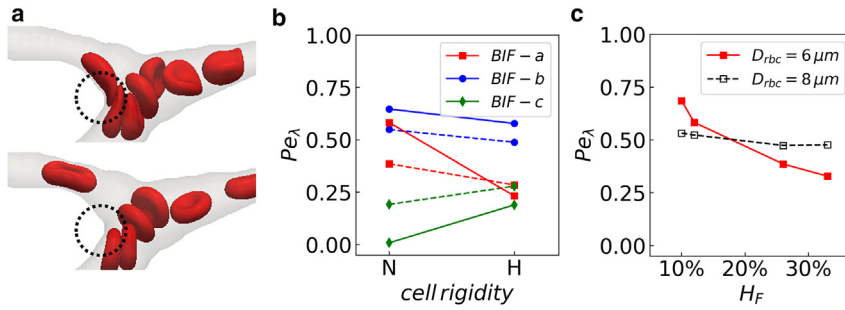

FIGURE 6 Potential origin of RBC lingering. (*a*) Schematic highlighting the flow split and the stagnation point at bifurcations. Flow in the mother branch splits into flows Q_{MD} and Q_{SD} in the MD and SD branches, respectively. The stagnation point is indicated by the green point, whose distance from the apex L_s is highlighted with the arrow and scale symbol. The filled circle shows an idealized cross section of the mother vessel with simplified and flat flow separatrix. (*b*) Correlation of the lingering Péclet number Pe_λ with the curvature ζ of the bifurcation at the stagnation point. (*c*) Correlation between Pe_λ and the flow rate ratio between the SD and MD Q_{SD}/Q_{MD}. (*d*) Correlation between Pe_λ and the distance between the stagnation point and the bifurcation apex L_S. (*e*) Correlation between L_S and the curvature at the stagnation point ζ. In (*b*)–(*e*), the points are experimental data, the solid lines show linear regression fitting of the data points, and the shaded areas indicate the 95% confidence interval prediction from each fit. To see this figure in color, go online. Error bars in (*b*–*e*) are computed by error propagation from the underlying experimental measurements.

FIGURE 7 Effect of cell rigidity and feeding hematocrit H_F on the lingering of RBCs in simulations. (*a*) Steric repulsion for (top) normal (N) and (bottom) hardened (H) RBCs at the apex of a Y-type bifurcation corresponding to BIF-a in Fig. 2. (*b*) Pe_λ versus cell rigidity for normal and hardened RBCs at BIF-a, BIF-b, and BIF-c" (see Fig. 2). Solid lines are for simulations with H_F matching corresponding experimental condition, whereas dashed lines are simulations with elevated hematocrit levels (twice as high for BIF-a and BIF-b, and three times as high for BIF-c). (*c*) Pe_λ versus feeding hematocrit H_F for BIF-a with normal RBCs (in deformability) of two different sizes $D_{rbc} = 6, 8$ μ m. To see this figure in color, go online.

(see Fig. S4). The curvature is defined as the inverse of the radius of this circle. To estimate the measurement uncertainty, we used multiple fitted circles, each calculated using a different length of the neighborhood (lengths between 4 and 8 μm, centered on the stagnation point). The mean value of the curvatures is taken as the best approximation, whereas the standard deviation gives the error bars. The results showed that the curvature of the bifurcation at the stagnation point correlates with Pe_λ ($r = 0.59$ and $p = 0.09$) (see Fig. 6 *b*). Interestingly, when testing correlations with further possibly influencing parameters, we found that the lingering Péclet number Pe_λ also correlates with the ratio of the flow rates between the SD and MD Q_{SD}/Q_{MD} (Fig. 6 *c*). Since this parameter determines the distance L_S between the apex of the bifurcation and the stagnation point through Eq. 4, this parameter L_S also correlates with Pe_λ (Fig. 6 *d*). Furthermore, the bifurcations where the stagnation point is further from the apex generally have a lower curvature at the stagnation point, as shown by Fig. 6 *e*.

We therefore hypothesize that the flow rate ratio determines where the cells can linger, whereas the curvature of the endothelial layer at this lingering position determines the intensity of the lingering. The lingering Péclet number would then be determined by an interplay between global parameters of the bifurcation (Q_{SD}/Q_{MD}) and local geometries of the endothelial layer (the curvature at the stagnation point, ζ). When it comes to the experimental correlations, the result that a lower coefficient is found between Pe_λ and ζ than Pe_λ and Q_{SD}/Q_{MD} likely arises from the fact that the determination of ζ also relies on the approximation for L_S and then the measurement of Q_{SD}/Q_{MD}. The error propagation on these successive quantities then likely decreased artificially the correlation between Pe_λ and the successively determined parameters L_S and ζ.

More geometrical parameters, which failed to demonstrate a significant correlation with Pe_λ, are included in the Supporting material (see Fig. S6).

Effect of cell rigidity and hematocrit in simulations

Besides the curvature of the stagnation point at the apex, other factors may also affect the interaction between the cells and the bifurcation, leading to either weakened or enhanced RBC lingering. Taking a typical Y-type bifurcation for example (Fig. 7 *a*), three physiologically relevant aspects were numerically explored: the cell rigidity κ_s, the feeding hematocrit H_F, and the cell size D_{RBC} ($D_{rbc} = 6$ μm unless otherwise specified).

Increased cell rigidity (imitating diseased RBCs with higher-level stiffness) at the Y-type bifurcation is found to introduce strong cell-wall and cell-cell steric repulsion at the apex (see enlarged gaps near the branching point in Fig. 7 *a*), thus reducing the overall lingering frequency and average duration of individual lingering events as indicated by a smaller lingering Péclet number Pe_λ (BIF-a in Fig. 7 *b*). The same is found for BIF-b too (Fig. 7 *b*). Contrarily, for a T-type bifurcation (less common bifurcation type in microvascular networks), stiffer RBCs tend to get stuck at the apex due to cell collisions and can lead to more intense lingering instead (see BIF-c in Fig. 7 *b*). The distinct effect of RBC deformability on its lingering behavior at the Y-type and T-type bifurcations observed here is in line with a recent report on capillary vascular network (30).

On the other hand, for identical flow conditions, an enriched hematocrit ($H_F = 33\%$, relative to the baseline $H_F = 12\%$ based on experimental measurement) in the M branch has a weakening effect on RBC lingering at the bifurcation, whereas a reduced hematocrit ($H_F = 10\%$) has a strengthening effect compared with the experimentally measured value $H_F = 12\%$ for the same bifurcation (Fig. 7 *c*). The probable reason behind the decreased Pe_λ in this case is that crowded cell traffic reduces the possibility of individual RBCs residing on the apex for extended periods of time as they are more likely to be pushed forward by following cells ("herding" effect as reported in (47)). We also considered a different RBC size given the variability of cell morphology in vivo, which is modeled through increasing the default cell diameter $D_{RBC} = 6$ μm from $D_{RBC} = 6$ μm to $D_{RBC} = 8$ μm while maintaining the same H_F (Fig. 7 *c*). The increased RBC size leads to higher level of cell confinement in the capillaries and reduces the fluctuation amplitude of RBC lingering caused by hematocrit alteration.

CONCLUSIONS

Our study demonstrates, for the first time in vivo, that RBC lingering (i.e., cells temporarily residing near the bifurcation apex with diminished velocity) constitutes an effective mechanism that significantly modifies the partitioning of cells through capillary bifurcations. Therefore, it should be taken into account when predicting the hematocrit distribution in microvascular networks using simplistic mathematical models based on existing empirical laws.

Existing literature has extensively tested and validated the Zweifach-Fung effect in microvascular bifurcations at the arteriolar level, mostly through microfluidic experiments or numerical simulations. Nonetheless, studies that experimentally quantify in vivo the effect of RBC-bifurcation interactions are rare, and it remains largely unknown how well the classic Pries-Secomb model describes the RBC partitioning at the excessively confined capillary level (12,30), where the cell-free layer (a key constituent in the empirical model of Pries et al. (22–24)) becomes negligible and the cells virtually squeeze through vessels in close contact. Previous numerical-experimental studies suggested that the branching geometry and cross sections of the daughter branches can indeed bias the partitioning of capsules at a bifurcation, depending on the size and deformability of the capsule (48). Considering much higher confinement reflecting capillary blood flow, our study represents the first in vivo demonstration of the microscopic effect of the bifurcation's local geometric feature and provides a mechanistic justification through intense cell-wall interactions, namely lingering, on the partitioning of RBCs.

Furthermore, we have shown that RBC lingering is inherently associated with a certain degree of asymmetry between the daughter branches (Fig. 5), which can either weaken the intrinsic Zweifach-Fung effect (thus rescuing disadvantaged low-flow branches and reducing unnecessary RBC-devoid vessels in the microvasculature), or reinforce it (thus enhancing advantageous high-flow branches and exacerbating the hematocrit heterogeneity on the network level). Indeed, Fig. S7 illustrates that both positive and negative deviations from the empirically predicted partitioning by Pries et al. (24) can be observed at a high lingering Péclet number. A similar trend is observed for deviations from the linear scaling (which hypothesizes that the fractional erythrocyte flow rate equals the fractional blood flow rate $FQ_e = FQ_b$; see Fig. S7). The key finding is that the lingering phenomenon is a prevalent mechanism in the capillary network, subject to fine-tuning of the fractional blood flows and geometrical features of the bifurcation. We demonstrate that, under the assumption of plug flow given highly confined cell motion, the lingering Péclet number (Pe_λ) correlates with the flow rate ratio Q_{SD}/Q_{MD}. This ratio Q_{SD}/Q_{MD} determines the position of the stagnation point, where the local curvature is further associated with the lingering intensity.

Our findings on the modulating effect of RBC lingering on hematocrit distribution have important implications for remodeling of the microvascular network occurring in development or reintroduced in disease. Recently, it has been uncovered that RBC distribution is strongly associated with the pattern of vascular remodeling, presumably by affecting the wall shear stress difference in neighboring branches through effective blood viscosity (21). Since lingering can substantially influence the RBC partitioning at capillary bifurcations (in extreme cases revert it), one can expect that lingering may play a key role in shaping the microcirculatory network, possibly contributing to the alterations of vascular networks as observed, e.g., in aneurysms and tumors. Additionally, since the deformability of RBCs affects their characteristic lingering time and, consequently, their partitioning, lingering might be a route through which the microvascular blood flow is impaired in diseases involving hardening of RBCs, such as malaria and sickle-cell disease (31–33,36–38). Further in vivo investigations with rigidified RBCs should be performed in future studies to test this hypothesis experimentally.

Finally, this work highlights the need for more models dedicated to RBC studies considering high confinement, as observed in microcirculatory environments entailing the lingering phenomena. Our results underline the importance of input parameters, such as the flow split at the bifurcation and the curvature of the apex region of the bifurcation.

SUPPORTING MATERIAL

Supporting material can be found online at https://doi.org/10.1016/j.bpj.2023.03.020.

AUTHOR CONTRIBUTIONS

A.D., C.W., M.W.L., L.K., and M.D.M. designed the research. G.S., M.W.L., and M.D.M. designed, applied, and obtained authorizations for animal experiments. G.S. and M.W.L. performed the surgery and recorded the videos. Y.R., A.D., A.K., M.B., and T.J. designed, implemented, and curated the analysis methods for experimental videos. Q.Z. designed the simulation and performed the numerical analysis with input from T.K. and M.O.B. Y.R., A.D., Q.Z., and G.S. wrote the manuscript. All authors discussed the results and critically reviewed the article.

ACKNOWLEDGMENTS

Rashidi et al.

DECLARATION OF INTERESTS

The authors declare no competing interests.

REFERENCES

1. Svanes, K., and B. Zweifach. 1968. Variations in small blood vessel hematocrits produced in hypothermic rats by micro-occlusion. *Microvasc. Res.* 1:210–220.

2. Fung, Y. C., and B. W. Zweifach. 1971. Microcirculation: mechanics of blood flow in capillaries. *Annu. Rev. Fluid Mech.* 3:189–210.

3. Schmid-Schönbein, G. W., R. Skalak, …, S. Chien. 1980. Cell distribution in capillary networks. *Microvasc. Res.* 19:18–44.

4. Pries, A. R., K. Ley, and P. Gaehtgens. 1986. Generalization of the Fahraeus principle for microvessel networks. *Am. J. Physiol.* 251:H1324–H1332.

5. Sherwood, J. M., D. Holmes, …, S. Balabani. 2014. Spatial distributions of red blood cells significantly alter local haemodynamics. *PLoS One.* 9:e100473.

6. Roman, S., A. Merlo, …, S. Lorthois. 2016. Going beyond 20 um-sized channels for studying red blood cell phase separation in microfluidic bifurcations. *Biomicrofluidics.* 10:034103.

7. Shen, Z., G. Coupier, …, T. Podgorski. 2016. Inversion of hematocrit partition at microfluidic bifurcations. *Microvasc. Res.* 105:40–46.

8. Clavica, F., A. Homsy, …, D. Obrist. 2016. Red blood cell phase separation in symmetric and asymmetric microchannel networks: effect of capillary dilation and inflow velocity. *Sci. Rep.* 6:36763.

9. Kaliviotis, E., J. M. Sherwood, and S. Balabani. 2017. Partitioning of red blood cell aggregates in bifurcating microscale flows. *Sci. Rep.* 7:44563.

10. Mantegazza, A., F. Clavica, and D. Obrist. 2020. In vitro investigations of red blood cell phase separation in a complex microchannel network. *Biomicrofluidics.* 14:014101.

11. Mantegazza, A., M. Ungari, …, D. Obrist. 2020. Local vs. global blood flow modulation in artificial microvascular networks: effects on red blood cell distribution and partitioning. *Front. Physiol.* 11:566273.

12. Pskowski, A., P. Bagchi, and J. D. Zahn. 2021. Investigation of red blood cell partitioning in an in vitro microvascular bifurcation. *Artif. Organs.* 45:1083–1096.

13. Hyakutake, T., H. Abe, …, Y. Tsutsumi. 2022. In vitro study on the partitioning of red blood cells using a microchannel network. *Microvasc. Res.* 140:104281.

14. Barber, J. O., J. P. Alberding, …, T. W. Secomb. 2008. Simulated two-dimensional red blood cell motion, deformation, and partitioning in microvessel bifurcations. *Ann. Biomed. Eng.* 36:1690–1698.

15. Xiong, W., and J. Zhang. 2012. Two-dimensional lattice Boltzmann study of red blood cell motion through microvascular bifurcation: cell deformability and suspending viscosity effects. *Biomech. Model. Mechanobiol.* 11:575–583.

16. Yin, X., T. Thomas, and J. Zhang. 2013. Multiple red blood cell flows through microvascular bifurcations: cell free layer, cell trajectory, and hematocrit separation. *Microvasc. Res.* 89:47–56.

17. Hyakutake, T., and S. Nagai. 2015. Numerical simulation of red blood cell distributions in three-dimensional microvascular bifurcations. *Microvasc. Res.* 97:115–123.

18. Ye, T., L. Peng, and G. Li. 2019. Red blood cell distribution in a microvascular network with successive bifurcations. *Biomech. Model. Mechanobiol.* 18:1821–1835.

19. Liu, Z. L., J. R. Clausen, …, C. K. Aidun. 2020. Heterogeneous partition of cellular blood-borne nanoparticles through microvascular bifurcations. *Phys. Rev. E.* 102:013310.

20. Triebold, C., and J. Barber. 2022. Dependence of red blood cell dynamics in microvessel bifurcations on the endothelial surface layer's resistance to flow and compression. *Biomech. Model. Mechanobiol.* 21:771–796.

21. Zhou, Q., T. Perovic, …, M. O. Bernabeu. 2021. Association between erythrocyte dynamics and vessel remodelling in developmental vascular networks. *J. R. Soc. Interface.* 18:20210113.

22. Pries, A. R., K. Ley, …, P. Gaehtgens. 1989. Red cell distribution at microvascular bifurcations. *Microvasc. Res.* 38:81–101.

23. Pries, A. R., T. W. Secomb, …, J. F. Gross. 1990. Blood flow in microvascular networks. Experiments and simulation. *Circ. Res.* 67:826–834.

24. Pries, A. R., B. Reglin, and T. W. Secomb. 2003. Structural response of microcirculatory networks to changes in demand: information transfer by shear stress. *Am. J. Physiol. Heart Circ. Physiol.* 284:H2204–H2212.

25. Balogh, P., and P. Bagchi. 2017. Direct numerical simulation of cellular-scale blood flow in 3D microvascular networks. *Biophys. J.* 113:2815–2826.

26. Zhou, Q., J. Fidalgo, …, T. Krüger. 2021. Emergent cell-free layer asymmetry and biased haematocrit partition in a biomimetic vascular network of successive bifurcations. *Soft Matter.* 17:3619–3633.

27. Chang, S.-S., S. Tu, …, M. Roper. 2017. Optimal occlusion uniformly partitions red blood cells fluxes within a microvascular network. *PLoS Comput. Biol.* 13:e1005892.

28. Balogh, P., and P. Bagchi. 2018. Analysis of red blood cell partitioning at bifurcations in simulated microvascular networks. *Phys. Fluids.* 30:051902.

29. Kihm, A., S. Quint, …, C. Wagner. 2021. Lingering dynamics in microvascular blood flow. *Biophys. J.* 120:432–439.

30. Ebrahimi, S., and P. Bagchi. 2022. A computational study of red blood cell deformability effect on hemodynamic alteration in capillary vessel networks. *Sci. Rep.* 12:4304.

31. Stuart, J., and G. B. Nash. 1990. Red cell deformability and haematological disorders. *Blood Rev.* 4:141–147.

32. Symeonidis, A., G. Athanassiou, …, N. Zoumbos. 2001. Impairment of erythrocyte viscoelasticity is correlated with levels of glycosylated haemoglobin in diabetic patients. *Clin. Lab. Haematol.* 23:103–109.

33. Dondorp, A. M., M. Nyanoti, …, K. Marsh. 2002. The role of reduced red cell deformability in the pathogenesis of severe falciparum malaria and its restoration by blood transfusion. *Trans. R. Soc. Trop. Med. Hyg.* 96:282–286.

34. Shevkoplyas, S. S., T. Yoshida, …, M. W. Bitensky. 2006. Direct measurement of the impact of impaired erythrocyte deformability on microvascular network perfusion in a microfluidic device. *Lab Chip.* 6:914–920.

35. Mohandas, N., and P. G. Gallagher. 2008. Red cell membrane: past, present, and future. *Blood.* 112:3939–3948.

36. Mannino, R., D. R. Myers, …, W. Lam. 2012. Increased erythrocyte rigidity is sufficient to cause endothelial dysfunction in sickle cell disease. *Blood.* 120:818.

37. Rabe, A., A. Kihm, …, L. Kaestner. 2021. The erythrocyte sedimentation rate and its relation to cell shape and rigidity of red blood cells from chorea-acanthocytosis patients in an off-label treatment with dasatinib. *Biomolecules.* 11:727.

38. Reichel, F., M. Kräter, …, J. Guck. 2022. Changes in blood cell deformability in chorea-acanthocytosis and effects of treatment with dasatinib or lithium. *Front. Physiol.* 13:1–11.

39. Laschke, M. W., B. Vollmar, and M. D. Menger. 2011. The dorsal skinfold chamber: window into the dynamic interaction of biomaterials with their surrounding host tissue. *Eur. Cell. Mater.* 22:147–164, discussion 164-167.

40. Xu, X., S. Xu, L. Jin, and E. Song. 2011. Characteristic analysis of Otsu threshold and its applications. *Pattern Recogn. Lett.* 32:956–961.

41. Sbalzarini, I. F., and P. Koumoutsakos. 2005. Feature point tracking and trajectory analysis for video imaging in cell biology. *J. Struct. Biol.* 151:182–195.

42. Bernabeu, M. O., M. L. Jones, …, C. A. Franco. 2018. PolNet: a tool to quantify network-level cell polarity and blood flow in vascular remodeling. *Biophys. J.* 114:2052–2058.

43. Sugii, Y., R. Okuda, …, H. Madarame. 2005. Velocity measurement of both red blood cells and plasma of in vitro blood flow using high-speed micro PIV technique. *Meas. Sci. Technol.* 16:1126–1130.

44. Secomb, T. W. 2017. Blood flow in the microcirculation. *Annu. Rev. Fluid Mech.* 49:443–461.

45. Jiang, X. Z., M. S. Goligorsky, and K. H. Luo. 2021. Cross talk between endothelial and red blood cell glycocalyces via near-field flow. *Biophys. J.* 120:3180–3191.

46. Chien, S., C. D. Tvetenstrand, …, G. W. Schmid-Schönbein. 1985. Model studies on distributions of blood cells at microvascular bifurcations. *Am. J. Physiol.* 248:H568–H576.

47. Barber, J. O., J. M. Restrepo, and T. W. Secomb. 2011. Simulated red blood cell motion in microvessel bifurcations: effects of cell–cell interactions on cell partitioning. *Cardiovasc. Eng. Technol.* 2:349–360.

48. Wang, Z., Y. Sui, …, W. Wang. 2018. Path selection of a spherical capsule in a microfluidic branched channel: towards the design of an enrichment device. *J. Fluid Mech.* 849:136–162.